16th Australasian Fluid Mechanics Conference
Crown Plaza, Gold Coast, Australia
2-7 December 2007

Assessment of Effect of Bubble Departure Frequency in Forced Convection Subcooled Boiling

R. Situ[1], J.Y. Tu[2], G.H. Yeoh[3], T. Hibiki[4], G.C. Park[5]

[1]Department of Engineering System
Queensland University of Technoloty, Bribane, Queensland, 4000 AUSTRALIA

[2]School of Aerospace, Mechanical & Manufacturing Engineering
RMIT University, Bundoora, Victoria, 3083 AUSTRALIA

[3]Australian Nuclear Science and Technology Organization
Menai, New South Wales, 2234, Australia

[4]School of Nuclear Engineering
Purdue University, West Lafayette, Indiana, 47907 USA

[5]Department of Nuclear Engineering
Seoul National University, Seoul, 151-742 Korea

Abstract

Bubble departure frequency is one of the important parameters for the prediction of subcooled flow boiling. This present work aims at an assessment of bubble departure frequency by investigating the physical mechanisms of three-dimensional two-fluid model coupled with the population balance equation. The CFX MUltiple-SIze-Group (MUSIG) model is used to predict bubbly flows with the presence of heat and mass transfer processes, particularly in subcooled boiling flows at low pressures. The assessment is carried out for these three models/correlations. The test shows that Podowski et al.'s model, with reasonable physical characteristics, is more realistic than the other two models when compared with the experimental data. The numerical results indicate that the higher the departure frequency, the lower the wall temperature and so the nucleation site density. In addition it is found that for both the axial and radial cases the curves of the void fraction tend to decrease with increase in departure frequency. The benchmark of the current numerical simulation with experimental data in both axial and radial profiles achieves successful agreement.

1. Introduction

Nucleate boiling has been extensively utilized in industry because it is one of the most efficient heat transfer modes, particularly in high energy density systems of nuclear reactor power plants. In the past several decades, much effort has been directed toward determining the relationship between heat flux and surface superheat for a particular material, with less progress achieved on the understanding of the nucleate boiling mechanisms, especially the nucleation site interaction mechanisms. Given the current state-of-the-art formulation, it can be acknowledged that the two-fluid model [1] when combined with the interfacial area transport equation or bubble number density transport equation would categorically proffer a highly developed and accurate analysis of thermal-hydraulic characteristics for industrial flow systems. Recently, the population balance approach for bubble number density transport equation has been considered towards solving the complex hydrodynamics. Several numerical studies, using the methodology of computational fluid dynamics (CFD), have been conducted [2,3]. The coupling between the CFD and population balance models has expedited a more thorough understanding of different flow regimes. They have also further enhanced a better understanding of the bubble mechanisms, especially with the consideration of bubble coalescence and breakup mechanisms in the model simulations. Although considerable efforts have been invested to develop more sophisticated models for bubble migration, attention of the transport processes is still very much focused on isothermal bubbly flow problems.

Hibiki and Ishii [4] formulated an interfacial area transport equation for two-phase turbulent flows. This transport equation may be regarded as a simpler form of the population balance equation in determining the range of bubble sizes in the flow volume. Along similar developments, Milles and Mewes [5] and Lehr and Mewes [6] formulated a transport equation for the interfacial area concentration to resolve the bubble mechanistic behaviors in bubble columns. Whilst adiabatic bubbly flow simulation has gain significant progress, modeling of subcooled boiling flow, which belongs to a specific category of bubbly flows, still remains a demanding task. Subcooled boiling flows are by nature a complex boiling process and behave very differently from isothermal bubbly flows. The flow involves hydrodynamics, heat and mass transfer, and bubbles undergoing coalescence and breakage; all of them are dynamically interacting within one single boiling process. In addition, the bubble growth, sliding, and lift-off at the heated surface contribute significantly towards modelling void growth and heat transfer.

In our past comprehensive investigation on axial void fraction distribution in vertical annulus channels, good agreement of the boiling flow model has been achieved against a wide range of experimental data[7]. The use of population balance and two-fluid models for gas–liquid bubbly flows is demonstrated through the implementation of the multiple sized-group (MUSIG) boiling model [8]. The latter solves a series of additional equations to accommodate the range of bubble sizes that exist within the two-phase flow volume. A complex MUSIG boiling model is employed to handle gas–liquid bubbly flows with heat and mass transfer. Because of the successes in using the population balance approach, the potential to implement and extend the modelling to examine the non-uniform bubble size distribution in subcooled boiling flows is of enormous significance. Therefore, a successful and specific development of the population balance approach for boiling flows can contribute to a significant improvement in formulation of the two-fluid boiling model.

The successful simulation of subcooled boiling flow using MUSIG boiling model demands accurate modelling of individual mechanisms, such as bubble departure mechanism, which forms the vital boundary condition for the bubble number density transport equation. The wall nucleation term in MUSIG model consists of three major parameters: active nucleation site density, bubble departure diameter, and bubble departure frequency. In CFX MUSIG modelling, the prediction of bubble departure

frequency may influence the prediction of wall superheat, thus affect the prediction of bubble departure diameter and active site density. Hence the proper choice of bubble departure frequency model might influence the overall CFD simulation.

Having dealt with the brief background of the previous researches, the current research mainly focuses on

(1) The development and formulation of a complete 3-D flow numerical simulation for subcooled boiling flows at low pressures. This is solved with a generic computer code CFX.

(2) An assessment of three models in literature such as Cole[9] and Basu et al. [10], and Podowski et al. [11].

An evaluation to validate the multiple-size group (MUSIG) model with new departure frequency model against experimental measurements. In addition, assessments of the model predictions for a particular mass flow rate, heat fluxes and inlet subcooled temperatures were also performed against local radial measurements of void fraction, Sauter mean diamter and interfacial area concentration.

2. Mathematic Model

2.1. Flow equation

The numerical simulations presented are based on the two-fluid model Eulerian–Eulerian approach. The Eulerian modelling framework is based on ensemble-averaged mass, momentum and energy transport equations for each phase. With the liquid phase (α_f) as continuum and the gaseous phase (bubbles) as dispersed phase (α_g), these equations can be written as

Continuity equation of liquid phase

$$\frac{\partial \rho_f \alpha_f}{\partial t} + \nabla \cdot (\rho_f \alpha_f \vec{u}_f) = \Gamma_{fg}, \quad (1)$$

Continuity equation of vapour phase

$$\frac{\partial \rho_g \alpha_g f_i}{\partial t} + \nabla \cdot (\rho_g \alpha_g \vec{u}_g f_i) = S_i - f_i \Gamma_{fg}, \quad (2)$$

Momentum equation of liquid phase

$$\frac{\partial \rho_f \alpha_f \vec{u}_f}{\partial t} + \nabla \cdot (\rho_f \alpha_f \vec{u}_f \vec{u}_f) = -\alpha_f \nabla P + \alpha_f \rho_f \vec{g} + \nabla \cdot \{\alpha_f \mu_f^e [\nabla \vec{u}_f + (\nabla \vec{u}_f)_t]\} + (\Gamma_{fg} \vec{u}_g - \Gamma_{gf} \vec{u}_f) + F_{fg} \quad (3)$$

Momentum equation of vapour phase

$$\frac{\partial \rho_g \alpha_g \vec{u}_g}{\partial t} + \nabla \cdot (\rho_g \alpha_g \vec{u}_g \vec{u}_g) = -\alpha_g \nabla P + \alpha_g \rho_g \vec{g} + \nabla \cdot \{\alpha_g \mu_g^e [\nabla \vec{u}_g + (\nabla \vec{u}_g)_t]\} + (\Gamma_{gf} \vec{u}_f - \Gamma_{fg} \vec{u}_g) + F_{gf} \quad (4)$$

Energy equation of liquid phase

$$\frac{\partial \rho_f \alpha_f H_f}{\partial t} + \nabla \cdot (\rho_f \alpha_f \vec{u}_f H_f) = \nabla \cdot [\alpha_f \lambda_f^e \nabla T_f] + (\Gamma_{fg} H_g - \Gamma_{gf} H_f) \quad (5)$$

Energy equation of vapour phase

$$\frac{\partial \rho_g \alpha_g H_g}{\partial t} + \nabla \cdot (\rho_g \alpha_g \vec{u}_g H_g) = \nabla \cdot [\alpha_g \lambda_g^e \nabla T_g] + (\Gamma_{gf} H_f - \Gamma_{fg} H_g) \quad (6)$$

In Eq. (1), Γ_{fg} represents the mass transfer rate attributed to condensation in the bulk subcooled liquid, which is expressed by

$$\Gamma_{fg} = \frac{h a_i (T_s - T_f)}{h_{fg}} \quad (7)$$

where h, a_i, T_s, and h_{fg} are the inter-phase heat transfer coefficient (determined from Ranz and Marshall) Nusselt number correlation, interfacial area concentration, saturation temperature, and latent heat, respectively. The wall vapour generation rate is modelled in a mechanistic way, derived by considering the total mass of bubbles detaching from the heated surface as

$$\Gamma_{gf} = \frac{Q_e}{h_{fg} + C_{pf} \Delta T_{sub}}, \quad (8)$$

where, Q_e, C_{pf}, and ΔT_{sub} are the heat transfer resulting from evaporation, liquid specific heat and liquid subcooling, respectively. This wall nucleation rate is accounted in Eq. (2) as a specified boundary condition apportioned to the discrete bubble class based on the size of the bubble departure criteria on the heated surface. On the right-hand side of Eq. (2), S_i represents the additional source terms attributed to coalescence and breakup based on the formulations that are described in the next section. The term $f_i \Gamma_{fg}$ represents the mass transfer resulting from condensation redistributed for each of the discrete bubble classes. The gas void fraction along with the scalar fraction f_i are related to the number density of the discrete bubble ith class n_i (similarly to the jth class n_j) as $\alpha_g f_i = n_i v_i$, where v_i is the volume of the ith class bubble. The size distribution of the dispersed phase is therefore defined by the scalar f_i. The population balance equation for each of the discrete bubble classes n_i is provided in the next section. Inter-phase transfer terms in the momentum and energy equations Γ_{fg} and F_{fg} denote the transfer terms from the gas phase to the liquid phase. The mass transfer Γ_{fg} is already given in Eq. (7), whereas the total interfacial force F_{fg} considered in the present study includes the effects of

$$F_{fg} = F_{fg}^{drag} + F_{fg}^{lift} + F_{fg}^{lubrication} + F_{fg}^{dispersion} \quad (9)$$

The total interfacial force F_{fg} is composed of the drag force, lift force, wall lubrication force and the turbulent dispersion force respectively. A detailed description of these forces and the corresponding force coefficients are detailed by Yeoh and Tu [12].

The k-ε turbulence model is used for the liquid and dispersed vapour continuum. The effective viscosity in the momentum and energy equations is taken as the sum of the molecular viscosity and turbulent viscosity. The turbulent viscosity is considered as the total of the shear-induced turbulent viscosity and Sato et al.'s [13] bubble-induced turbulent viscosity.

The wall heat flux Q_w is composed of three components: the heat transferred by conduction to the superheated layer next to the wall, Q_q; the heat transferred by evaporation or vapour generation, Q_e; and the heat transferred by turbulent convection, Q_c. Details of the wall heat flux is provided by Yeoh and Tu [12]. The local bubble Sauter mean diameter based on the calculated values of the scalar fraction f_i and discrete bubble sizes d_i is calculated by:

$$D_{sm} = 1 \Big/ \sum_i f_i / d_i \,. \quad (10)$$

2.2. Bubble Coalescence, Break up, and Condensation Models

Pohorecki et al. (2001) suggested dividing the population balance equation into N classes to classify the range of bubble sizes that may be present within the flow volume, *viz.*,

$$\frac{\partial n_i}{\partial t} + \nabla \cdot \left(\vec{u}_g n_i\right) = \left(\sum_j R_j\right)_i + \left(R_{ph}\right)_i \quad (11)$$

where $(\sum_j R_j)_i$ (= $P_C + P_B - D_C - D_B$) represents the net change in the number density distribution due to coalescence and breakup processes. This interaction term contains the source rates of P_C, P_B, D_C and D_B, which are respectively, the production rates due to coalescence and breakup and the death rate to coalescence and breakup of bubbles. The bubble coalescence is modelled using Prince and Blanche's model [14] whereas the bubble breakup adopts Luo and Svendsen's model [15]. The term $(R_{ph})_i$ in Eq. (11) comprises the essential formulation of the source/sink rates for the phase change processes associated with subcooled boiling

flow. At the heated surface, bubbles form at activated cavities known as active nucleation sites. The bubble nucleation rate from these sites will be discussed in Section 2.3. The bubble sink rate due to condensation in a control volume for each bubble class can be determined from:

$$\phi_{\mathrm{COND}} = -\frac{n_{\mathrm{i}}}{V_{\mathrm{b}}} A_{\mathrm{b}} \frac{h\left(T_{\mathrm{sat}} - T_{\mathrm{l}}\right)}{\rho_{\mathrm{g}} h_{\mathrm{fg}}} \tag{12}$$

Given that the bubble surface area A_b and volume V_b based on the bubble Sauter diameter are respectively πD_s^2 and $\pi D_s^3/6$, Eq. (12) can be rearranged as:

$$\left(R_{\mathrm{ph}}\right)_{\mathrm{i}} = \phi_{\mathrm{COND}} = -\frac{1}{\rho_{\mathrm{g}} \alpha_{\mathrm{g}}} \left[\frac{h a_{\mathrm{i}} \left(T_{\mathrm{sat}} - T_{\mathrm{f}}\right)}{h_{\mathrm{fg}}}\right] n_{\mathrm{i}} \tag{13}$$

2.3. Modelling of Wall Nucleation Terms

The wall nucleation terms can be expressed by

$$\phi_{\mathrm{wn}} = N_{\mathrm{a}} f_{\mathrm{d}} \xi_{\mathrm{h}} / A_{\mathrm{c}} \tag{14}$$

where N_a, ξ_h, A_c are active nucleation site density, heated perimeter, and cross-sectional area of the flow channel, respectively. Since the bubble nucleation process only occurs at the heated surface, this heated wall nucleation rate is not included in $(R_{ph})_i$ but rather specified as a boundary condition to Eq. (11) apportioned to the discrete bubble class n_i based on the bubble departure criteria on the heated surface.

The active nucleation site density is expressed by the correlation by Lemmert and Chwalas [16]:

$$N_{\mathrm{a}} = \left[210\left(T_{\mathrm{w}} - T_{\mathrm{s}}\right)\right]^{1.805} \tag{15}$$

A total of there models of bubble departure frequency are implemented in MUSIG model in this study. At first bubble departure frequency correlation of Cole [9] was taken into consideration, which was developed from buoyancy-drag force balance theory for pool boiling of water, CCl_4, and methanol data with the averaged error of ±52.2%.

$$f = \sqrt{\frac{4g\left(\rho_{\mathrm{f}} - \rho_{\mathrm{g}}\right)}{3 D_{\mathrm{d}} \rho_{\mathrm{f}}}} \tag{16}$$

where g is the gravitational acceleration. The bubble departure diameter D_d is formulated from considering the balance of surface tension and buoyancy forces at low pressures.

$$D_{\mathrm{d}} = 2.496 \times 10^{-5} \left(\frac{\rho_{\mathrm{f}} - \rho_{\mathrm{g}}}{\rho_{\mathrm{g}}}\right)^{0.9} \theta \left[\frac{\sigma}{g\left(\rho_{\mathrm{f}} - \rho_{\mathrm{g}}\right)}\right]^{0.5} \tag{17}$$

where θ and σ are the contact angle and surface tension respectively.

Basu et al. [10] measured both the waiting time, t_W, and the growth time, t_G, for subcooled boiling flow in vertical channels with mass flux from 235.0 to 684.0 kg/m^{2}s, inlet subcooling from 7.7 ~ 46.5 °C, and heat flux from 200.0 ~ 454.0 kW/m^2. The waiting time was correlated with wall superheat as

$$t_{\mathrm{W}} = 139.1\left(\Delta T_{\mathrm{w}}^{-4.1}\right). \tag{18}$$

The growth time was correlated with bulk subcooling, bubble departure diameter, and superheated liquid layer:

$$\frac{D_{\mathrm{d}}^2}{\alpha_{\mathrm{f}} Ja_{\mathrm{sup}} t_{\mathrm{G}}} = 45 \exp\left(-0.02 Ja_{\mathrm{sub}}\right) \tag{19}$$

where $Ja_{sup}=\rho_f C_{pf}\Delta T_w/\rho_g h_{fg}$, and $Ja_{sub}=\rho_f C_{pf}\Delta T_{sub}/\rho_g h_{fg}$. Once t_G and t_W are known, the bubble departure frequency was calculated by

$$f_{\mathrm{d}} = 1/\left(t_{\mathrm{W}} + t_{\mathrm{G}}\right). \tag{20}$$

Podowski et al. [12] proposed a mechanistic model of bubble departure frequency for forced convection subcooled boiling. The bubble waiting time is therefore given by

$$t_{\mathrm{W}} = \left[\left(-C_2 + \sqrt{C_2^2 - 4C_1C_3}\right)\Big/ 2C_1\right]^2, \tag{21}$$

where $C_1 = 2q''_{\mathrm{w}}/R\pi$,

$$C_2 = T_i\left(0^+\right) - T_{\mathrm{s}} - \frac{q''_{\mathrm{w}} r_{\mathrm{c}}}{R\sqrt{\pi\alpha_{\mathrm{f}}}} - \frac{2\sigma}{r_{\mathrm{c}}} \frac{T_{\mathrm{s}} v_{\mathrm{fg}}}{i_{\mathrm{fg}}}, \quad \text{and}$$

$C_3 = -\left[T_{\mathrm{i}}\left(0^+\right) - T_{\mathrm{b}}\right] r_{\mathrm{c}} / \sqrt{\pi\alpha_{\mathrm{f}}}$. v_{fg} is specific volume change during evaporation of liquid (=1/ρ_g–1/ρ_f), and

$$R = k_{\mathrm{w}} / \sqrt{\pi\alpha_{\mathrm{w}}} + k_{\mathrm{f}} / \sqrt{\pi\alpha_{\mathrm{f}}}, \tag{22}$$

where k_w and α_w are thermal conductivity and thermal diffusivity of wall, respectively. $T_i(0^+)$ is the instantaneous wall surface temperature at time 0^+

$$T_{\mathrm{i}}\left(0^+\right) = \left(\frac{k_{\mathrm{w}} T_{\mathrm{w}}}{\sqrt{\alpha_{\mathrm{w}}}} + \frac{k_{\mathrm{f}} T_{\mathrm{b}}}{\sqrt{\alpha_{\mathrm{f}}}}\right) \Bigg/ \left(\frac{k_{\mathrm{w}}}{\sqrt{\alpha_{\mathrm{w}}}} + \frac{k_{\mathrm{f}}}{\sqrt{\alpha_{\mathrm{f}}}}\right). \tag{23}$$

In this present study the cavity radius, r_c, is set as 10^{-5} m is used to simplify the calculation.

Once the waiting time is calculated the bubble departure frequency is calculated by $f_d=1/t_W$. The growth time was neglected in this calculation because it is two or three order smaller than the waiting time.

3. Experiment details

Two datasets of local flow parameters experiments, and two datasets of axial flow parameter experiments, whose test condition are presented in Table 1, were compared with simulation results.

Table 1. Experimental conditions.

Researcher	Case	P_{in} [MPa]	T_{in} [°C]	Q_w [kW/m^2]	G [kg/m^{2}s]
Lee et al	L1	0.142	96.6	152.9	474.0
Lee et al	L2	0.137	95.0	197.2	714.4
Zeitoun & Shoukri	A1	0.150	94.6	508.0	264.3
Zeitoun & Shoukri	A2	0.168	95.7	603.2	403.1
Situ et al.	LA1	0.129	95.0	151.0	630.74
Situ et al.	LA2	0.133	95.0	150.1	1183.93

For the local measurements performed by Lee et al.[17], the experimental setup consisted of a vertical concentric annulus with an inner heating rod of 19 mm outer diameter. The heated section was a 1.67 m long Inconel 625 tube with 1.5 mm wall thickness and filled with magnesium oxide powder insulation. The rod was uniformly heated by a 54 kW DC power supply. The outer wall comprised of two stainless steel tubes with 37.5 mm inner diameter. The plane for measuring the radial distribution was located at 1.61 m downstream of the beginning of the heated section. Demineralised water was used as the working fluid. Local gas phase parameters such as local void fraction, bubble frequency and bubble velocity were measured by a two-conductivity probe method. The bubble Sauter diameters (assuming spherical bubbles) were determined through the IAC, calculated using the measured bubble velocity spectrum and bubble frequency.

For the axial measurements performed by Zeitoun and Shoukri [18], the test section was a vertical concentric annular test section. The inner tube, which had a 12.7 mm outside diameter, was a 30.6 cm long, thick-walled stainless-steel tube (0.25 mm thick) that was electrically heated. The entire inner tube was connected to a 55kW DC power supply. The outer tube

was a 25.4 mm inner diameter plexiglass tube that permitted visual observation. Distilled-degassed water was used as the working fluid. A digital image processing technique was used to analyze the high-speed video information and to measure bubble size distributions along the subcooled boiling region. A single beam gamma densitometer was used for the void fraction measurements.

For the local-axial measurement performed by Situ et al. [18], the experimental setup consisted of a vertical concentric annulus with an inner heating rod of 19.05 mm outer diameter. The heated section was a 1.73 m long transparent polycarbonate tube with 38.1 mm inner diameter and 3.18 mm wall thickness. The maximum power of the heater is 20 kW, and has a maximum surface heat flux of 0.193 MW/m^2. The local flow measurements using the double-sensor conductivity probe were performed at four axial locations of z_h/D_H =31.3, 52.6, 68.7, and 89.4 as well as 12 radial locations from $r/(R_o-R_i)$=0.05 to 0.95 under the atmospheric pressure condition. Here, z_h and D_H are the axial distance from the start point of heating and the hydraulic equivalent diameter, respectively, and r, R_o, and R_i are the radial location measured from the heater rod surface, the inner radius of the outer tube, and the outer radius of the heater rod, respectively. Local gas phase parameters such as void fraction, Sauter mean diameter, interfacial area concentration, and interfacial velocity were measured by a two-conductivity probe method. The area-averaged values of these gas phase parameters were also obtained by using Spline function.

4. Numerical Procedures

The set of conservation equations were discretized using the finite control volume technique. The discrete bubble sizes, prescribed in the dispersed phase, were further tracked by solving an additional set of 15 transport equations, which were progressively coupled with the flow equations during the simulations. The velocity–pressure linkage was handled through the SIMPLE procedure. The discretized equations were solved using Stone's Strongly Implicit Procedure [20]. Since the wall heat flux was applied uniformly throughout the inner wall of the annulus, the advantage of the annular geometrical shape was used by modelling only one quarter of the annulus as the domain for simulation for both the local and axial cases.

A body-fitted conformal system was used to generate the three-dimensional mesh within the annular channel, resulting in a total of 13 (radial) x 30 (height) x 3 (circumference) control volumes for the local case (L1, L2), whereas a total of 10 (radial) x 20 (height) x 3 (circumference) control volumes resulted for the axial case (A1, A2), and a total of 10 (radial) x 60 (height) x 3 (circumference) control volumes for the local-axial case (LA1, LA2). Because wall function was used in the present study, the normal distance between the wall and the first node in the bulk liquid should be such that the corresponding y^+ was greater than 30. In addition grid independence was examined. In the mean parameters considered, further grid refinement did not reveal significant changes to the two-phase flow parameters. Convergence was achieved within 1500 iterations when the mass residual dropped below 1 x 10^{-7}. As the global execution time also dependent on the amount of data the computer wrote to the hard disk, on an average it took 30 minutes on a Pentium III machine.

5. Results and Discussions

5.1. Frequency effect on Wall Nucleation Term

In investigating the effect of bubble departure frequency on the performance of the numerical simulation, wall temperature is found to be a crucial parameter, because wall temperature has close relationship with bubble departure frequency and active nucleation site density. In general more bubble departure frequency causes more bubble generation, thereby contributing to more evaporation heat flux into the bulk fluid thus resulting in lower wall temperature, which will cause lower active nucleation site density, as suggested by Eq. (15). Since the wall nucleation term is proportional to the power of bubble departure frequency and active nucleation site density, the impact of active nucleation site density should also be considered in discussing the change of wall nucleation term.

At first several arbitrary values of bubble departure frequencies from 10 to 500 s^{-1} are tested for L1 and L2 cases. Bubble departure frequencies outside of the 10-500 s^{-1} range are considered not realistic. Figure 1 plot the wall superheat, active nucleation site density, and wall nucleation terms against bubble departure frequency at three locations, z_h/D_H=1.5, 43.6, and 88.8. The drawn curves suggest that as the increase of bubble departure frequency, wall superheat will decrease, so does active nucleation site densities. However, the curves of wall nucleation terms first decrease and then increase with the growing of bubble departure frequency.

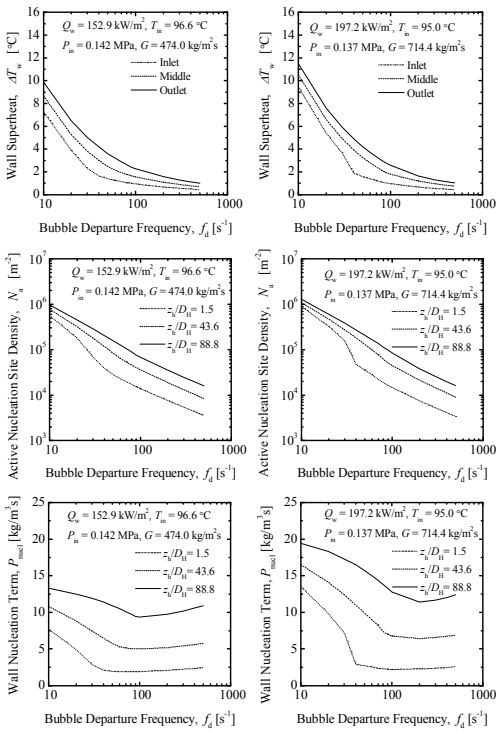

Figure 1. Effect of bubble departure frequency.

Next the axial profiles of the bubble departure frequencies predicted by Cole, Basu et al., and Podowski et al. are compared along the heated surface and the plots of which are shown in Figure 2. From the interpretation it could be seen that the curve of Cole's correlation is constant along the flow direction. The obvious reason is that the correlation of Cole is only dependent on the fluid properties and bubble departure diameter, however, the values of which are also determined by fluid properties in the present code. Further it is seen that the curve of Basu et al.'s correlation increases, however, insignificantly from 11 to16 s^{-1} in case L1. On the other hand the model by Podowski et al. showed an increase in bubble departure frequency from 28 to 53 s^{-1} for case L1. As an understanding, along the flow direction both the wall temperature and the liquid temperature increases, as these are directly proportional to the bubble departure frequency, the bubble departure frequency increases as well. It is therefore understood that the prediction of Cole's correlation, which is derived from pool boiling data, is not physically sound. The curve obtained for Basu et al.'s correlation does show an increase; however, the prediction is too small and thus can not be considered realistic. Whilst Podowski et al. model predicts departure frequency to be less than 100 for low heat flux cases

(L1, L2, LA1, LA2), and to be between 200 and 500 s^{-1} for high heat flux cases (A1, A2). It is also noted that for case LA2, the departure frequency in section less than 0.3 m is zero. This is because it is still single phase flow in the heat beginning section.

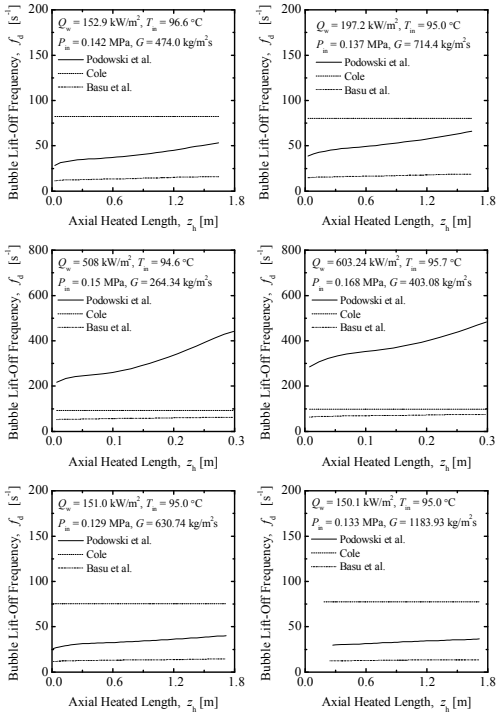

Figure 2. Axial profile of bubble departure frequency.

As it was established that the bubble departure frequency has a relationship with the wall temperature, the prediction of bubble departure frequency is expected to have a profound effect on the prediction of the wall temperature. The plots of which are shown as wall superheat temperatures in Figure 3. As seen, in case L1, L2, and LA1, the prediction of Cole increases from 1 to 3 °C, the wall super heat of Basu is in the range of 6 to 7 °C and the prediction by Podowski et al. lies between Cole and Basu with an increase from 2 to 4 °C. However, in case A1 and A2, the prediction of Podowski et al., Cole, and Basu et al. are in the range of 3 to 4 °C, 6 to11 °C and 10 to 12 °C, respectively. The wall superheat at the beginning section in case LA2 is negative due to the high subcooling.

Furthermore, it is observable that the variation of wall superheat will affect the prediction of nucleation site density. The nucleation site density is shown to be increasing with the developing of heated length, as shown in Figure 4. It should be taken into consideration that the nucleation site density is proportional to the power of 1.805 times the wall superheat. Thus even a few degrees of temperature difference in the wall superheat will produce significant divergence in nucleation site density. In saying so, the prediction by Basu et al. is found to the highest in the three models. The prediction of Situ et al is higher than the prediction of Cole in cases L1, L2, LA1, and LA2, and less for cases A1 and A2.

Finally, the axial profiles of wall nucleation terms are plotted with axial heated length for all the six cases in figure 5. Not surprisingly, the wall nucleation terms increase with the growth of heated length. In addition, comparison of these three bubble departure frequency models reveals that the higher the prediction of bubble departure frequency model results in the lower wall nucleation terms. Since Basu et al.'s correlation predicts the lowest bubble departure frequency for all the six cases, the corresponding wall nucleation terms are the highest among the three models. Between the other two models, Cole's correlation gives higher departure frequency and lower wall nucleation terms for local and local-axial cases, while higher wall nucleation terms were obtained for axial cases. Although Figure 1 suggests that wall nucleation term is not a monotonously decreasing function of the bubble departure frequency, the wall nucleation terms do show decreasing trend with the rising of bubble departure frequency for the current test conditions and bubble departure frequency models.

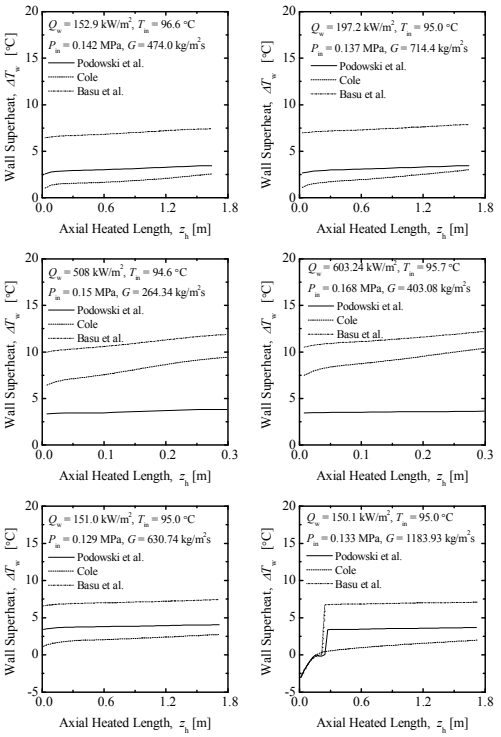

Figure 3. Axial profile of wall superheat.

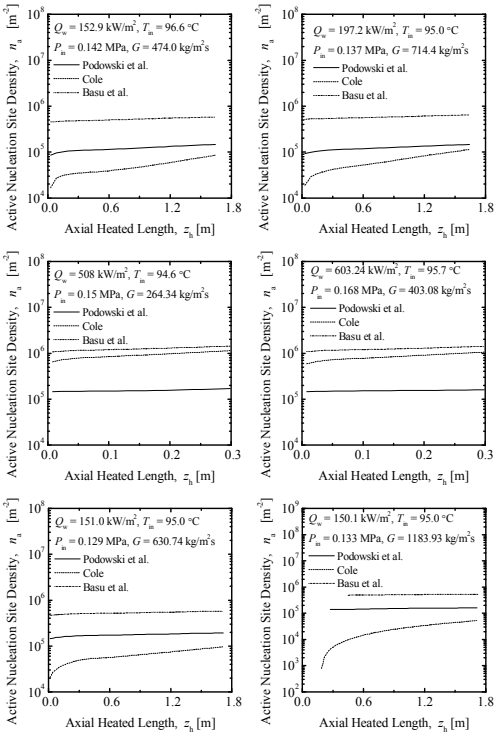

Figure 4. Axial profile of nucleate site density.

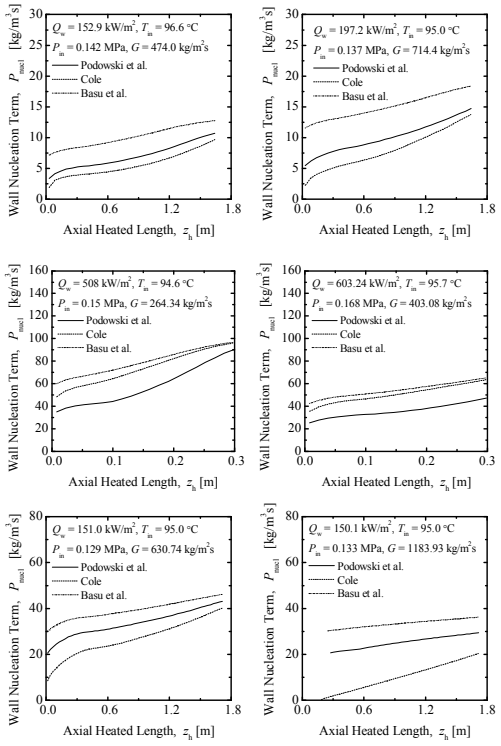

Figure 5. Axial profile of wall nucleation term.

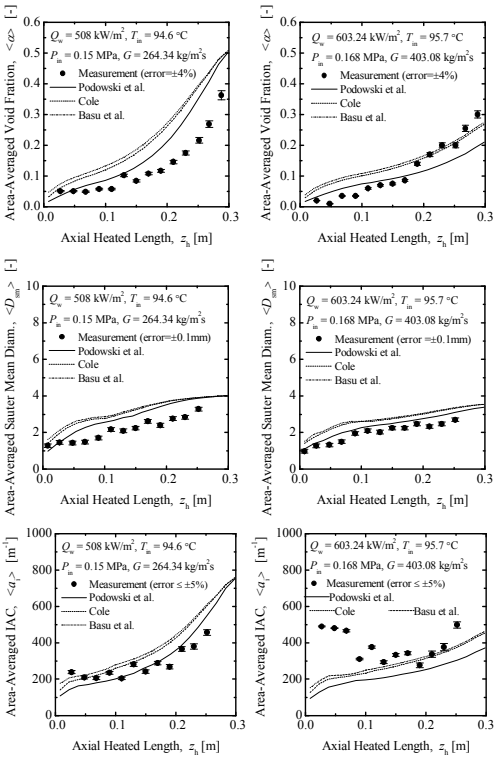

Figure 6. Axial profile of area-averaged flow parameter for cases A1 and A2.

5.2. Axial Profile of Area-Averaged Flow Parameters

As already mentioned in introduction, the wall nucleation term acts as the boundary condition for MUSIG model. Hence the variation in wall nucleation source term would affect the prediction of void fraction and other parameters. Though the assessment of the bubble departure frequency and its related terms were comprehensively illustrated, attention was also focussed in validating these models. In order to validate these models, the axial profiles of area-averaged void fraction, Sauter mean diameter and interfacial area concentration for the axial cases are shown in Figure 6. The experimental data are shown by symbol "●" with error bars, and the predicted values are represented by continuous curves. As expected, the curves of Basu et al's model are hierarchically the highest, and the prediction of Podowski et al. gives the lowest results. In addition, the differences for the three predicted axial profiles of area-averaged Sauter mean diameter are insignificant, because all the simulation chose the same bubble departure diameter model, which is determined by fluid properties and independent of bubble departure frequency model. For case A1, the simulations over-predict the void fraction profile. This might be due to the over-prediction of wall superheat, which also results in higher bubble coalescence and large Sauter mean diameter, as also suggested in Figure 6. The predictions of area-averaged interfacial area concentration have good agreement with data. While For case A2, Podowski et al's model have better agreement with data at upstream, while the models by Cole and Basu et al. have better agreement at downstream. All these three models over-predict the Sauter mean diameter, with Podowski's model give the best fitting. While for the axial profile of area-averaged IAC, the experimental data shows higher values at inlet, which is unrealistic. Actually the IAC data is not obtained from direct measurement, but from the measured values of void fraction and bubble size, by equation: $a_i = 6\alpha/D_{sm}$. Hence the measurement discrepancy may be augmented, and the first three points might not be reliable.

The axial profiles of area-averaged void fraction, Sauter mean diameter and interfacial area concentration for the local-axial cases are shown in Figures 7, where the symbol are the same as in Figure 6. The predicted curves show that although the highest and the lowest predictions are given by Basu et al.'s correlation and Cole's correlation respectively, all the three models predict similar values of void fraction and Sauter mean diameter. Additionally, the numerical simulations under-predict the Sauter mean diameter in both cases. For cases LA1 and LA2, the experimental data is averaged over the bubble layer, while the numerical prediction is estimated by averaging the Sauter mean diameter over the whole flow channel, and might introduce under-estimation. Furthermore, all the models over-estimate the area-averaged IAC for both cases. This is because the IAC is reciprocal to the Sauter mean diameter, and the under-prediction of Sauter mean diameter will cause the over-prediction of IAC.

For case LA1, the simulations of all three models agree excellent good with the data in the first three positions, while under-predict at the fourth position, where the void fraction data is higher than 40% and the flow becomes saturate slug flow. Because the current CFX model is developed for subcooled bubbly flow, its application extended in slug flow require more modification. In case LA2, the prediction curves are flat around 0.8 mm, which does not agree with the growing trend indicated by the experiment. This might be due to the choice of bubble coalescence model which under-predicts the bubble coalescence.

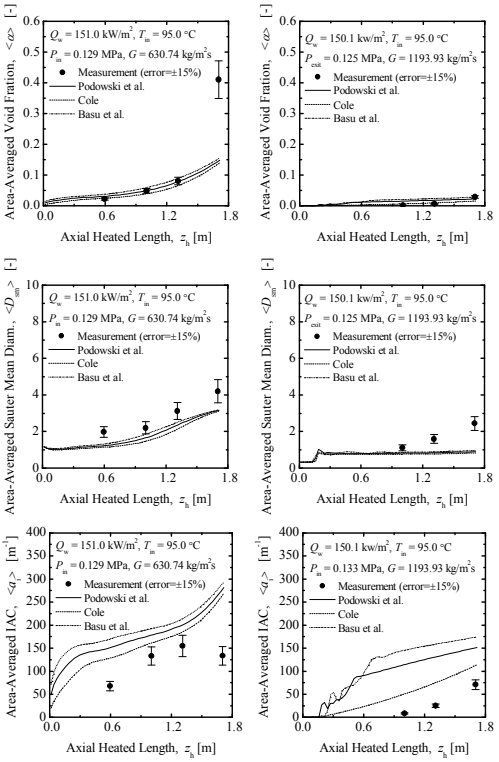

Figure 7. Axial profile of area-averaged flow parameter for cases LA1 and LA2.

5.3. Radial Profile of Flow Parameter

The local radial profiles of void fraction, Sauter mean diameter and the IAC for local cases L1 and L2 are plotted in Figure 8. The plot indicates Basu et al's prediction is the highest, while Cole's prediction is the lowest. For L1 case, all the three models over-predict the void fraction in the close vicinity of the heating surface, and the differences of these models are small. While for case L2, Basu et al's model over-predicts the void fraction, and the other two models agree well with the data. Moreover, for both cases, the models over-predict Sauter mean diameter at higher radial positions. This might due to the choice of bubble condensation model. Next the comparison between the measured and the predicted IAC depict similar trendline as the void fraction profile.

The local radial profiles of void fraction, Sauter mean diameter and the IAC for local-axial case LA1 are plotted in Figure 9. For case LA1, the three models fit well with data of void fraction and IAC in the first three positions. However, at the first radial position close to the heating surface, i.e., $(r-R_i)/(R_o-R_i) = 0.05$, the experimental data at $z_h/D_H = 52.6$ and 68.7 is small than the second position, as similar to case L1, whilst the model does not predict this trend. Study of local Sauter mean diameter see that the models over-predict in lower axial positions but fit well with experimental data at higher location, i.e., at $z_h/D_H = 68.7$. Furthermore, the predicted IAC profile shows similar trendline as the void fraction profile.

Figure 10 draws the local radial profiles of void fraction, Sauter mean diameter and the IAC for local-axial case LA2. The models over-predict the void fraction and interfacial area concentration at the first two locations but agree well at the third position. While for Sauter mean diameter, the models over-predict in the first two axial positions and under-predict in the last axial positions.

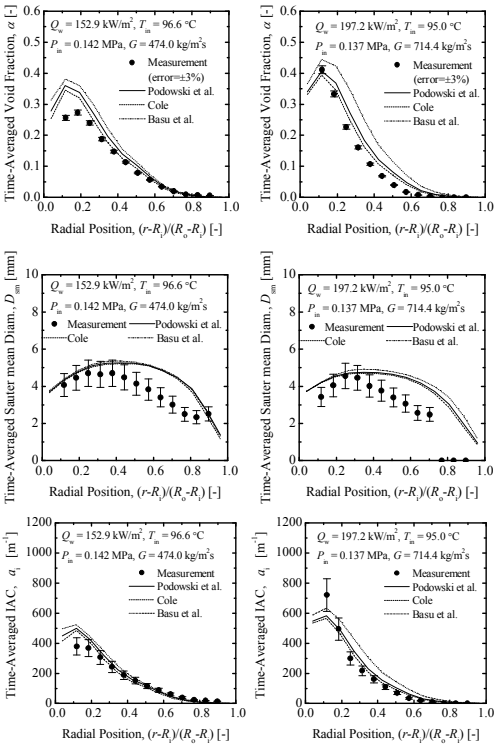

Figure 8. Radial profile of local flow parameter for cases L1 and L2.

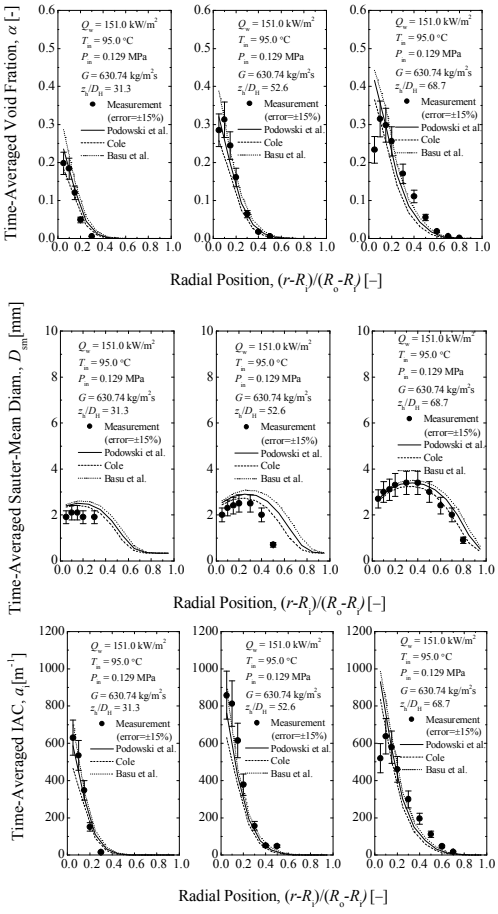

Figure 9. Radial profile of local flow parameters for LA1 case.

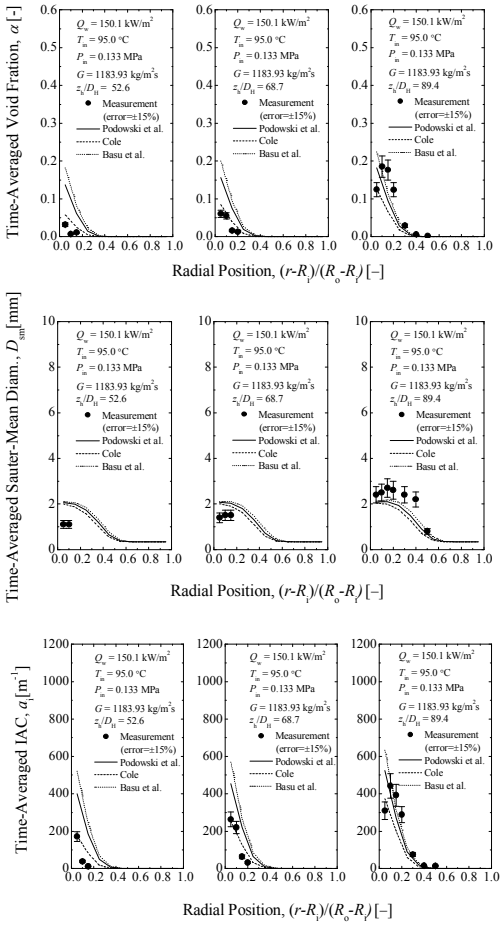

Figure 10. Radial profile of local flow parameters for LA2 case.

6. Conclusion

The numerical assessment of bubble departure frequency in subcooled boiling flow is conducted in the present study. Subcooled boiling flow comprises all the complex dynamic interaction of the phenomena associated with hydrodynamics, heat and mass transfer, and coalescence and breakup of bubbles. A two-fluid model coupled with population balance approach, i.e., the MUSIG boiling model, is proposed to handle wall nucleation on the heated surface, condensation process in the subcooled liquid core, bubble coalescence and breakup. Bubble departure frequency is one of the important parameter to determine the wall nucleation rate for subcooled flow boiling. In literature Cole's correlation is developed from pool boiling and only depends on liquid property, whereas Basu et al.'s recent correlation only represent their data without any comparison with any other models. In contrast, Podowski et al.'s mechanistic model takes account of transient heat conduction both in the heated material and liquid.

The assessment was carried out for these three models/correlations. The test shows that the Podowski et al.'s bubble departure frequency model has a higher growth rate along the flow direction when compared to the other two models, which is constant or insignificant. Thus it is suggested that Podowski et al.'s model, with reasonable physical characteristics, is more realistic than the other two models when compared with the experimental data. The numerical results indicates that the higher the departure frequency, the lower the wall temperature and so the nucleation site density. In addition it is found that for both the axial and radial cases the curves of the void fraction tend to decrease with increase in departure frequency. The benchmark of the current model with experimental data in both axial and radial profiles achieves successful agreement.

Acknowledgement

The research project was supported by Australian Research Council (ARC) Discovery Project DP0556094. The authors would like to express their sincere appreciation for the support.

References

[1] Ishii, M. And Hibiki, T., Thermo-fluid dynamics of two-phase flow, Springer, 2005.

[2] R. Krishna, M.I. Urseanu, J.M. van Baten, J. Ellenberger, Influence of scale on the hydrodynamics of bubble columns operating in the churn-turbulent regime: Experiments vs. Eulerian simulations. Chem. Eng. Sci. 54 (1999) 4903-4911.

[3] R. Pohorecki, W. Moniuk, P. Bielski, A. Zdrojkwoski, Modelling of the coalescence/re-dispersion processes in bubble columns. Chem. Eng. Sci. 56 (2001) 6157-6164.

[4] T. Hibiki, M. Ishii, Two-group area transport equations at bubbly-to-slug flow transition. Nucl. Eng. Des 202 (2000) 39-76.

[5] M. Milles, D. Mewes, Interfacial area density in bubbly flow. Chem. Eng. & Processing 38 (1999) 307-319.

[6] F. Lehr, D. Mewes, A transport equation for the interfacial area density applied to bubble columns. Chem. Eng. Sci. 56 (2001) 1159-1166.

[7] J.Y. Tu, and G.H. Yeoh, On numerical modelling of low-pressure subcooled boiling flows, Int. J. Heat and Mass Transfer 45 (2002) 1197-1209.

[8] G.H. Yeoh, and J.Y. Tu, A bubble mechanistic model for subcooled boiling flow predictions, Numerical Heat Transfer, Part B: Fundamentals 45 (2004) 475–493.

[9] R. Cole, A photographic study of pool boiling in the region of the critical heat flux. American Institute of Chemical Engineers 6 (1960) 533-542.

[10] N. Basu, G. R. Warrier, and V.K. Dhir, Wall heat flux partitioning during subcooled flow boiling: Part1 — Model development, J. Heat Transfer 127 (2005) 131-139.

[11] R. M. Podowski, D. A. Drew, R. T. Lahey, Jr., and M. Z. Podowski, A mechanistic model of the ebullition cycle in forced convection subcooled boiling, 8th International Topical Meeting on Nuclear Reactor Thermal-Hydraulics, Volume 3 (1997) 1535- 1542, Kyoto, Japan,.

[12] G.H. Yeoh, J.Y. Tu, Thermal-Hydraulic Modelling of Bubbly Flows with Heat and Mass Transfer, AIChE J. 51 (2005) 8-27

[13] Y. Sato, M. Sadatomi, K. Sekoguchi, Momentum and heat transfer in two-phase bubbly flow—I, Int. J. Multiphase Flow 7 (1981) 167-178.

[14] Prince M.J. and Blanch H.W. Bubble Coalescence and Break-up in Air-Sparged Bubble Column, AIChE J. 36 (1990) 1485-1499.

[15] H. Luo, H. Svendsen, Theoretical model for drop and bubble break-up in turbulent dispersions, AIChE J. 42 (1996) 1225-1233.

[16] Lemmert, M. and Chwala, J.M., Influence of flow velocity on surface boiling heat transfer coefficient, Adademic Press/Hemisphere, 1977.

[17] T.H. Lee, G.C. Park, D.J. Lee, Local flow characteristics of subcooled boiling flow of water in a vertical annulus, Int. J. Multiphase Flow 28 (2002) 1351–1368.

[18] O. Zeitoun, M. Shoukri, Bubble behavior and mean diameter in subcooled flow boiling, ASME J. Heat Transfer 118 (1996) 110-116.

[19] R. Situ, T. Hibiki, X. Sun, Y.Mi, and M. Ishii, Axial development of subcooled boiling flow in an internally heated annulus, Exp. in fluids 37 (2004) 589-603.

[20] H.L. Stone, Iterative solution of implicit approximations of multidimensional partial differential equations, SIAM J. Num. Anal. 5 (1968) 530-558.